Geophysical Research Letters

RESEARCH LETTER
10.1029/2024GL114176

Predictability of Semiannual Atmospheric Circulation Type Frequencies in the Extratropics Using the EC-Earth3 Decadal Forecasting System

S. Brands[1], **E. Cimadevilla**[1], **and J. Fernández**[1]

[1]Instituto de Física de Cantabria (IFCA), CSIC-Universidad de Cantabria, Santander, Spain

Key Points:

- Significant skill is found in predicting the December-to-May frequencies of synoptic circulation types up to 13 months in advance
- On a hemispheric average, simulations initialized with observations outperform those driven solely by external forcing agents
- Actual predictability is virtually never significantly greater than potential predictability

Supporting Information:

Supporting Information may be found in the online version of this article.

Correspondence to:

S. Brands,
brandssf@ifca.unican.es

Citation:

Brands, S., Cimadevilla, E., & Fernández, J. (2025). Predictability of semiannual atmospheric circulation type frequencies in the extratropics using the EC-Earth3 decadal forecasting system. *Geophysical Research Letters*, *52*, e2024GL114176. https://doi.org/10.1029/2024GL114176

Received 10 DEC 2024
Accepted 15 MAY 2025

Author Contributions:

Conceptualization: S. Brands, J. Fernández
Data curation: S. Brands, E. Cimadevilla, J. Fernández
Formal analysis: S. Brands
Funding acquisition: J. Fernández
Investigation: S. Brands, J. Fernández
Methodology: S. Brands, J. Fernández
Project administration: S. Brands, J. Fernández
Resources: S. Brands, E. Cimadevilla
Software: S. Brands, E. Cimadevilla
Supervision: S. Brands, J. Fernández
Validation: S. Brands
Visualization: S. Brands
Writing – original draft: S. Brands, E. Cimadevilla

Abstract We investigate the skill of the fully initialized decadal forecasting system EC-Earth3 in re-forecasting the semiannual occurrence frequencies of synoptic-scale atmospheric circulation types in the extratropics. Six-hourly sea-level pressure data from 10 model integrations of the dcppA-hindcast experiment are transformed into discrete circulation-type time series using the Jenkinson-Collison approach. The frequencies of these types are then compared to those derived from a reference reanalysis. The resulting skill is assessed and compared to that of a 10-member ensemble run with historical forcing to evaluate the added value of initialization. In the Pacific-North American sector, both the skill and added value are significant for the December-to-May season of the first forecast year. In the Southern Hemisphere, significant results are found for the same season through the second forecast year and also for the June-to-November season of the first forecast year. Significant *signal-to-noise paradox* situations are virtually absent in the analyses conducted here.

Plain Language Summary This work is a pilot study on the near-term climate predictability of semiannual weather type frequencies in the extratropics, derived from sub-daily model and reanalysis data, which are primarily influenced by atmospheric noise. Contrary to expectations, significant predictability is found in both hemispheres up to 13 months in advance, particularly during the December-to-May season. At this forecast horizon, observation-based model initialization provides added value in most regions globally, including some where the actual skill is not significant. We conclude that decadal predictions are more suitable for making operational forecast decisions regarding atmospheric circulation than previously thought.

1. Introduction

Extratropical cyclones and anti-cyclones typically have lifetimes ranging from a few days to a few weeks. They can move in any cardinal direction, and their relative position to one another drives the atmospheric flow at any given location. This, in turn, determines the characteristics of the advected air masses, which can be classified using either subjective or objective methods (Chang et al., 2002; Philipp et al., 2010). The spatiotemporal variability of these transient eddies and weather regimes is large and generally stochastic in nature. On a background of enhanced noise, low-frequency variations in the atmosphere naturally occur due to energy flux integration from other climate system components, such as the ocean, sea-ice extent, snow cover, and surface albedo (often referred to as "internal" agents) and from external forcing agents, including solar activity, greenhouse gas concentrations, sulfate aerosols, and volcanic activity (Hasselmann, 1976; Mann et al., 2020). These factors vary more slowly than the atmosphere, on multiple timescales, making them more predictable. However, due to the predominance of high-frequency weather noise, detecting their influence on the atmosphere is challenging, and internal climate variability must be properly sampled in attribution studies (Gillett et al., 2016; Wills et al., 2022). The ratio of the signal exerted by these boundary climate system components to the unpredictable atmospheric noise is termed the *signal-to-noise ratio* (Hasselmann, 1979). This ratio is typically derived from an ensemble of coupled general circulation model (GCM) integrations, which are assumed to provide perfect surrogates of the real climate system. Higher values indicate greater predictability. The signal-to-noise ratio is generally higher in the ocean than in the atmosphere, and within the atmosphere, it is particularly low for circulation variables like sea-level pressure, when compared with temperature or precipitation (Deser et al., 2012). Consequently, the hindcast skill of initialized forecasting systems is generally limited to reproducing long-term trends caused by external forcing agents (primarily greenhouse gases) (Yeager & Robson, 2017). The *added skill*, which describes the improvement of initialized forecasts relative to non-initialized ones, particularly in forecasting internal (unforced) climate variability, is especially heterogeneous over continental land areas. Different forecasting

Writing – review & editing: S. Brands, E. Cimadevilla, J. Fernández

systems yield varying results in these regions (Bethke et al., 2021; Goddard et al., 2013). One key reason for the limited skill is that the signal derived from GCM ensembles is generally too weak and/or the noise component is too large, pointing to systematic model deficiencies (Baker et al., 2018; Eade et al., 2014).

The present study explores the skill of the full-field initialized decadal forecasting system EC-Earth3, run at the Barcelona Supercomputing Center (Bilbao et al., 2021), in its ability to reproduce the observed semiannual frequencies of recurrent atmospheric circulation types at sea level, represented by reanalysis data. This is done by applying the Jenkinson and Collison (1977) (JC) approach, also referred to as *Lamb Weather Types* (Lamb, 1972), a discrete classification scheme that transforms continuous sea-level pressure patterns over a given region into 11 distinct *circulation types*, each with a physical meaning and a discernible impact on surface weather conditions (Jones et al., 1993; Trigo & DaCamara, 2000). The JC approach is linked to the main modes of low-frequency atmospheric variability, such as the Arctic or North Atlantic Oscillation, but it describes the atmospheric circulation at a smaller, synoptic scale (Fernández-Granja et al., 2024). As such, it is more closely tied to surface weather and is more relevant for impact studies (Brands et al., 2014; Soares et al., 2019).

2. Data

We use 6-hourly instantaneous sea-level pressure (SLP) data from the decadal ensemble prediction system developed at the Barcelona Supercomputing Center (BSC). This system is based on the coupled general circulation model EC-Earth3 (Döscher et al., 2021), for which a dedicated data assimilation system was developed to allow for full-field forecast initialization (Bilbao et al., 2021). It participates in the Decadal Climate Prediction Project (DCPP), which focuses on the coordinated exploration of decadal climate predictability and the provision of initialized decadal predictions based on a multi-model approach (Boer et al., 2016). The DCPP experiment is part of the Coupled Model Intercomparison Project Phase 6 (CMIP6) (Eyring et al., 2016), and its "A-hindcast" component generates initialized retrospective forecasts (also known as hindcasts) from various ensemble prediction systems. For EC-Earth3, a 10-member ensemble of dcppA-hindcast (hereafter: dcppA) simulations was available at the time of writing the manuscript. These hindcasts are compared here with a 10-member ensemble of *historical* model integrations of the same GCM. The historical runs are initialized from distinct dates within a pre-industrial control run and are integrated with observed variations in external forcing from 1850 to 2015, including greenhouse gas concentrations, solar activity, aerosol load, volcanic activity, and other factors (Döscher et al., 2021). Unlike the dcppA runs, the historical runs are *not* constrained by observations of internal climate variability during the integration period (Meinshausen et al., 2017). As a result, these are typically referred to as "uninitialized" experiments, even though they are initialized from the pre-industrial control run. We chose EC-Earth3 primarily because of the comprehensive data availability from the Earth System Grid Federation (ESGF) and because its historical runs perform well in comparison with reanalysis data (Brands, 2022; Brands et al., 2023).

The retrospective dcppA forecasts were initialized annually on November 1st, starting from 1960 through 2018, and integrated over a forecast period of 11 years. These consecutive model initializations were concatenated to create semiannual, year-to-year time series on a 6-hourly time scale, with a constant lead-time throughout the hindcast period. We focus on the December-to-May (DJFMAM) and June-to-November (JJASON) seasons, having lead-times of 1 month and 7 months in the first forecast year (FY1), 13 and 19 months in FY2, and so on. This concatenation ensures that data for a given season and year is derived from the same initialization.

The historical simulations end in 2015. To enable comparison with the retrospective dcppA forecasts from 2016 onward, the historical simulations were concatenated with their corresponding SSP2-4.5 scenario simulations (Meinshausen et al., 2020). The resulting time series are referred to as "historical+." The common verification period available for all dcppA forecast years and the historical+ experiment is 1970–2019 (50 years). The exact specifications of the dcppA and historical+ EC-Earth3 runs used here are provided in Table S1 in Supporting Information S1. As a quasi-observational reference for model verification, we use the ECMWF Reanalysis version 5 (ERA5) (Hersbach et al., 2020). The CERA-20C reanalysis is used in addition (Laloyaux et al., 2018) to analyze the observational uncertainty by means of an example. While ERA5 is an atmospheric reanalysis that assimilates observations from a wide range of sources, CERA-20C is a coupled ocean-atmosphere reanalysis that only assimilates surface observations.

Using the *patch* method of Python's xESMF package (https://xesmf.readthedocs.io/), all SLP fields were interpolated to a regular 2.5° grid, which is required for applying the classification method described below.

3. Methods

3.1. The Jenkinson-Collison Classification Scheme of Atmospheric Circulation

The Jenkinson and Collison (1977) (JC) classification technique transforms continuous sea-level pressure (SLP) fields into 27 discrete circulation types, based on a subjective classification scheme initially developed by Lamb (1972) for the British Isles. This method uses a 16-point coordinate system that covers a 30° × 20° longitude-latitude area centered over the region of interest (Figure S1 in Supporting Information S1). Several circulation indices are calculated based on the meridional and zonal pressure gradients defined within this coordinate system. These indices are then classified using a set of rules to form the 27 types. Each type is associated with a specific vorticity condition (cyclonic or anticyclonic) and/or flow direction.

The 27 types include: 8 *pure directional* types, characterized by strong pressure gradients without a clear vorticity sign (NE, E, SE, S, SW, W, NW, N); 16 *hybrid* types, which occur when the aforementioned flow directions are accompanied by either cyclonic or anticyclonic conditions; one *pure cyclonic* type; one *pure anticyclonic* type; and one *unclassified* type, which is characterized by near-zero vorticity values and weak pressure gradients. Fernández-Granja et al. (2023) extended the JC method to be applicable to any location in the extratropics between 30° and 70° latitude, as suggested earlier by Jones et al. (2013).

As an illustrative example, Figure S1 in Supporting Information S1 shows the SLP composite maps for the method centered over Wellington, New Zealand. For simplicity and because many of the hybrid classes occur infrequently (Table S2 in Supporting Information S1, column 4), the original 27 JC types have been reduced to the 11 classes proposed by Serras et al. (2024). This reduction merges the hybrid-cyclonic, hybrid-anticyclonic, and pure directional types of a given cardinal direction into a single directional type, resulting in 8 directional types in total. The pure cyclonic, pure anticyclonic, and unclassified types remain unchanged (Table S2 in Supporting Information S1, columns 2 and 5).

3.2. Verification Measures

To measure the hindcast skill of the dcppA and historical EC-Earth3 experiments described in Section 2, we use the Pearson correlation coefficient between the semiannual ensemble-mean circulation type frequencies, which describe the forced response (or signal), and the corresponding frequencies from ERA5 (r_o) (Smith et al., 2019).

The added value (AV) of initialization from observations is defined as the difference between r_o obtained from the 10-member ensemble of dcppA runs (r_{dcppa}) and r_o obtained from the 10-member ensemble of historical runs (r_{hist}):

$$AV = r_{dcppa} - r_{hist} \tag{1}$$

If the correlation with the reanalysis is higher for the initialized runs than for the historical runs ($AV > 0$), it indicates that initialization from observations improves the correlation, thus providing added value.

The ratio of skill (also referred to as *actual* predictability) to the *potential* predictability obtained in the model world (i.e., from the 10-member EC-Earth3 ensembles of dcppA or historical runs) is termed the *Ratio of Predictable Components* (RPC):

$$RPC = r_o / r_m \tag{2}$$

where r_m is the average Pearson correlation coefficient between the ensemble-mean time series and the time series of the individual members (Cottrell et al., 2024).

Ideally, the ensemble-mean should correlate equally strongly with observations as with individual ensemble members, as the latter are assumed to be equally probable surrogates of the climate system's real evolution over time (Scaife & Smith, 2018). However, for initialized climate prediction systems in actual use, the ensemble-mean often correlates less strongly with observations than with the individual ensemble members, resulting in RPC values below 1. This situation is expected and can arise from: (a) sampling uncertainties in the ensemble-mean and spread estimates from a small number of members, (b) systematic errors in the predicted signals that would also appear in a large ensemble, or (c) shortcomings in the initialization procedure that cause sudden

physical inconsistencies (or shocks) leading to large shifts in the model output time series. RPC values exceeding 1 indicate that the individual model members do not serve as perfect surrogates for the real evolution of the climate system. This has several important implications, as summarized in Scaife and Smith (2018).

The significance of r_{dcppA} and r_{hist} is assessed using a two-tailed Student's t-test. The significance of AV or RPC is calculated using a two-tailed z-test on the Fisher-transformed values of r_{dcppa} and r_{hist}, or r_o and r_m, respectively (Wilks, 2006). The significance level for all tests is set at 5, and all statistics are computed for both raw and linearly de-trended time series. The corresponding differences are small, so only the results based on the de-trended time series are presented in Section 4.

4. Results

An illustrative example of the typical time series characteristics of the dcppA hindcast is shown in Figure S2 in Supporting Information S1. The dcppA ensemble-mean frequencies for the westerly circulation type over the Wellington area are plotted against corresponding quasi-observations from ERA5 and CERA-20C for DJFMAM 1960/61 to 2018/19. On the background of small observational uncertainties, the hindcasts are positively biased and substantially underestimate the observed inter-annual variability (panel a). Standardization corrects errors in mean and variance but does not affect the correlation coefficient (+0.36, panel b).

The grid-box-scale r_{dcppa} (columns 1 and 3) and AV (columns 2 and 4) values for the westerly circulation type are mapped in Figure 1. These two statistics are shown separately for FY1 and FY2, for DJFMAM and JJASON, and for the Northern and Southern Hemispheres (NH and SH). Significant positive correlation coefficients ($\alpha = 0.05$, two-tailed) are indicated by black dots. In the NH, significant skill is obtained from the dateline to the western North American coast during the DJFMAM season of FY1, including the northwestern U.S., southwestern Canada, central U.S., and the Arctic coastline of Canada and Alaska (Figure 1a). More isolated skill regions are observed in central Asia, southwestern Scandinavia, and France. For the JJASON season of FY1, significant skill is found only south of the Aleutians and around the Azores (panel c). During FY2, significant skill is virtually absent in the NH (e and g). A large area of significant skill is obtained over the vast ocean areas of the Southern Hemisphere's mid-to-high latitudes during DJFMAM in FY1 and FY2 (i and m), including land areas such as New Zealand (in both FY1 and FY2) and southeast Australia (FY2). During the JJASON season, the significant skill area shrinks considerably in FY1 (but persists over southern New Zealand) and virtually disappears in FY2 (k and o).

The skillful regions generally overlap with regions of added value, indicated by pattern correlation coefficients ranging from 0.63 to 0.71, provided in the upper-right corner of the panels shown in columns 2 and 4 of Figure 1. Notably, for the DJFMAM season in FY1 and particularly FY2, added value over the central-to-eastern subtropical Atlantic Ocean is significant, even where skill itself is not, but is near the critical value (compare a with b and e with f). Figure 1 also reveals regions of significant reduced value (or skill loss), such as southern Scandinavia and Ukraine during DJFMAM in FY2, and southeastern Spain during JJASON in FY2 (f and h). The corresponding results for the Pure Anticyclonic and Pure Cyclonic types are shown in Figures S3 and S4 in Supporting Information S1. From FY3 onwards, the hindcasts are generally not skillful, and corresponding results are not shown.

Figure 2 displays the spatial samples for the westerly circulation type (shown as maps in Figure 1) along with results for the remaining 10 circulation types. Each box plot represents a specific circulation type. As shown, skill and added value for the DJFMAM season in FY1 are displaced toward positive values for every circulation type in both hemispheres (a, b, i, and j), indicating robust (or systematic) results when considering hemispheric-wide perspectives rather than grid-box scale results. Similar results are observed for the DJFMAM season in FY2, but only in the SH (m and n). The largest spatial average skill value, indicated by the black horizontal line in the boxes, is obtained for the westerly circulation types in the SH (i, j, m, and n). The corresponding results for the JJASON season (columns 3 and 4) are generally centered around zero, indicating no skill or added value, except for the SH and FY1 (k and l), where the distributions shift slightly toward positive values.

Figure 3 shows the number of circulation types yielding significant skill (columns 1 and 3) or added value (columns 2 and 4), reflecting the degree to which the circulation type-specific results agree on the grid-box scale. This synthesis figure reveals additional land areas where the frequencies of 2–7 (out of 11) circulation types can be hindcast with significant skill during the DJFMAM season in FY1. These include Alaska and far eastern

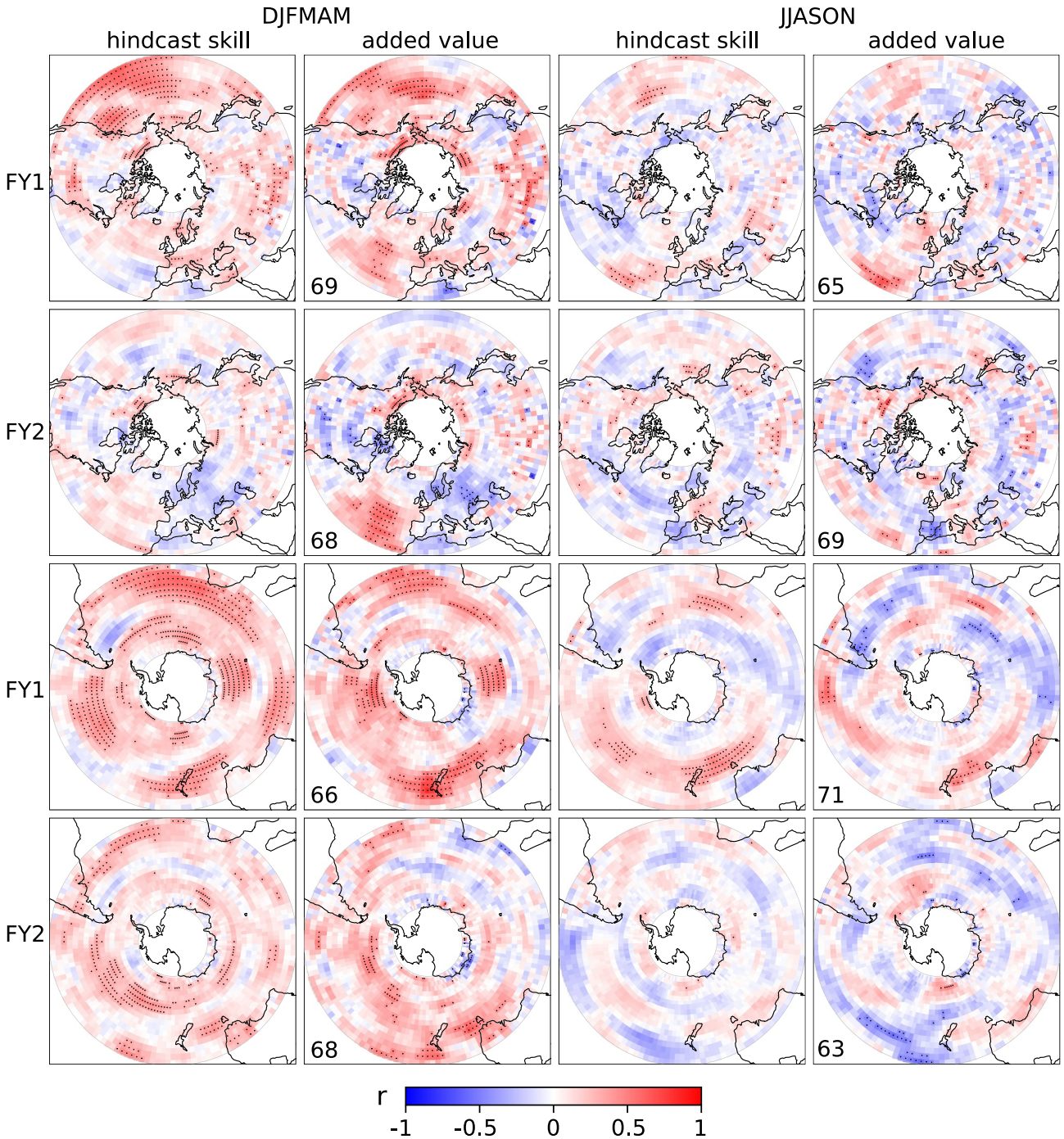

Figure 1. Column 1 and 3: Hindcast skill of the EC-Earth3 dcppA ensemble as measured by the Pearson correlation coefficient (r) between the ensemble-mean semiannual frequencies of westerly flow situations and quasi-observations from ERA5 for the DJFMAM and JJASON seasons in FY1 and 2. Column 2 and 4: As column 1 and 3, but for the added value of the dcppA ensemble compared to the historical ensemble. Black dots indicate significance ($\alpha = 0.05$). Rows 1 and 2: Results for the NH; Rows 2 and 4: Results for the SH. The pattern correlation coefficient (×100) between skill and added value is indicated in the lower left corner of the panels in columns 2 and 4.

Siberia, the southern U.S. and Mexico, and Italy in the NH (panel a), as well as South Africa, parts of Argentina and Central Chile, and southeast Australia in the SH (i). A relatively large agreement is also found over subtropical ocean areas of the SH and the Southern Ocean off the coast of Queen Maud Land. Remarkably, southeast Australia stands out as the only land region receiving significant hindcast skill for the DJFMAM season in both FY1 and FY2 (i and m). For the JJASON season, the synthesis analysis also reveals additional significant skill

10.1029/2024GL114176

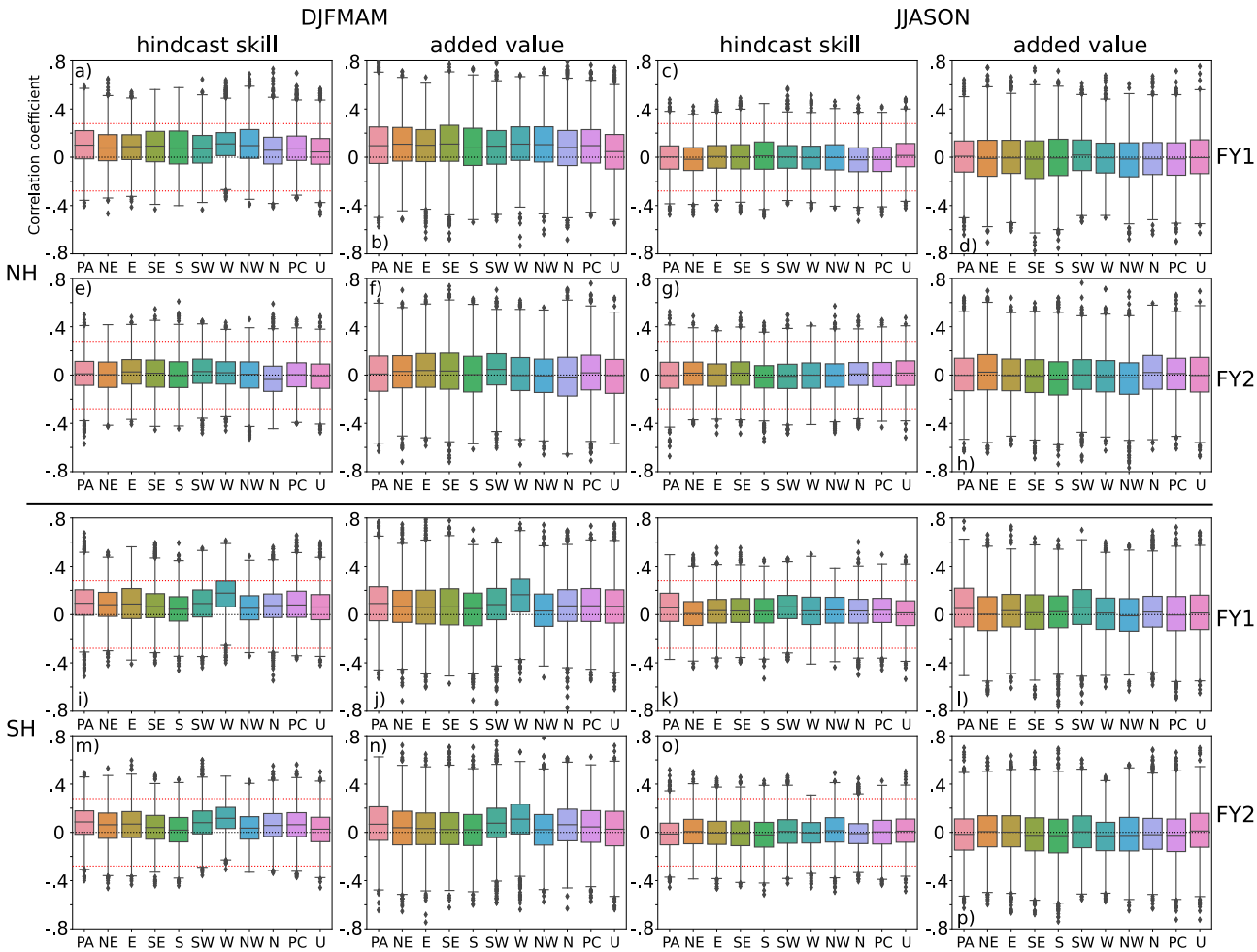

Figure 2. Columns 1 and 3: Spatial distribution of the grid-box scale values for hindcast skill and added value (*y*-axis) for all circulation types (*x*-axis). Separate panels are provided for FY1 and 2, the DJFMAM and JJASON seasons, and the NH and SH. Dashed horizontal lines indicate the critical value for a significant correlation coefficient. Each box-plot item shows the spatial median value and the inter-quartile range (IQR) of a given sample. Whiskers are set at the 3rd quartile +1.5 × IQR and at the 1st quartile - 1.5 × IQR of this sample.

areas over land, including southern Australia, East Antarctica, and Uruguay, but only for single circulation types and mostly restricted to FY1 (k), except over the Iberian Peninsula, where significant skill is obtained for a single type in both FY1 and FY2 (c and g).

The spatial patterns of added value agreement are similar to those for skill agreement (compare columns 2 and 4 with columns 1 and 3 in Figure 3), but weaker over the SH during DJFMAM in FY1 (compare i with j). A closer look reveals that the historical ensemble already provides significant skill for up to 3 circulation types in the Antarctic Subpolar Belt, off the coast of Queen Maud Land and East Antarctica (not shown), possibly due to circulation effects of stratospheric ozone forcing (Goyal et al., 2021).

The RPC values for the westerly circulation type in FY1 and FY2 of the dcppA ensemble, as well as the historical ensemble, are shown in Figure 4. As expected from the relatively small ensemble size, RPC values <1 (blue shading) are obtained over a large fraction of the study area in both hemispheres, across all lead times and seasons. RPC values >1, indicating a signal-to-noise paradox, rarely occur (red shading in Figure 4). For the 6-month frequency aggregations shown, actual predictability is never significantly larger than potential predictability. A significant paradox occurs only in very rare cases when 3-month frequencies are considered (not shown). Remarkably, the largest spatial average RPC value is obtained during the DJFMAM season in FY1 over the SH, coinciding with the largest average skill (compare Figure 1i with Figure 4g). The spatial RPC patterns correlate strongly with corresponding skill patterns (the first number in the lower-left corner of the panels in Figure 4) and

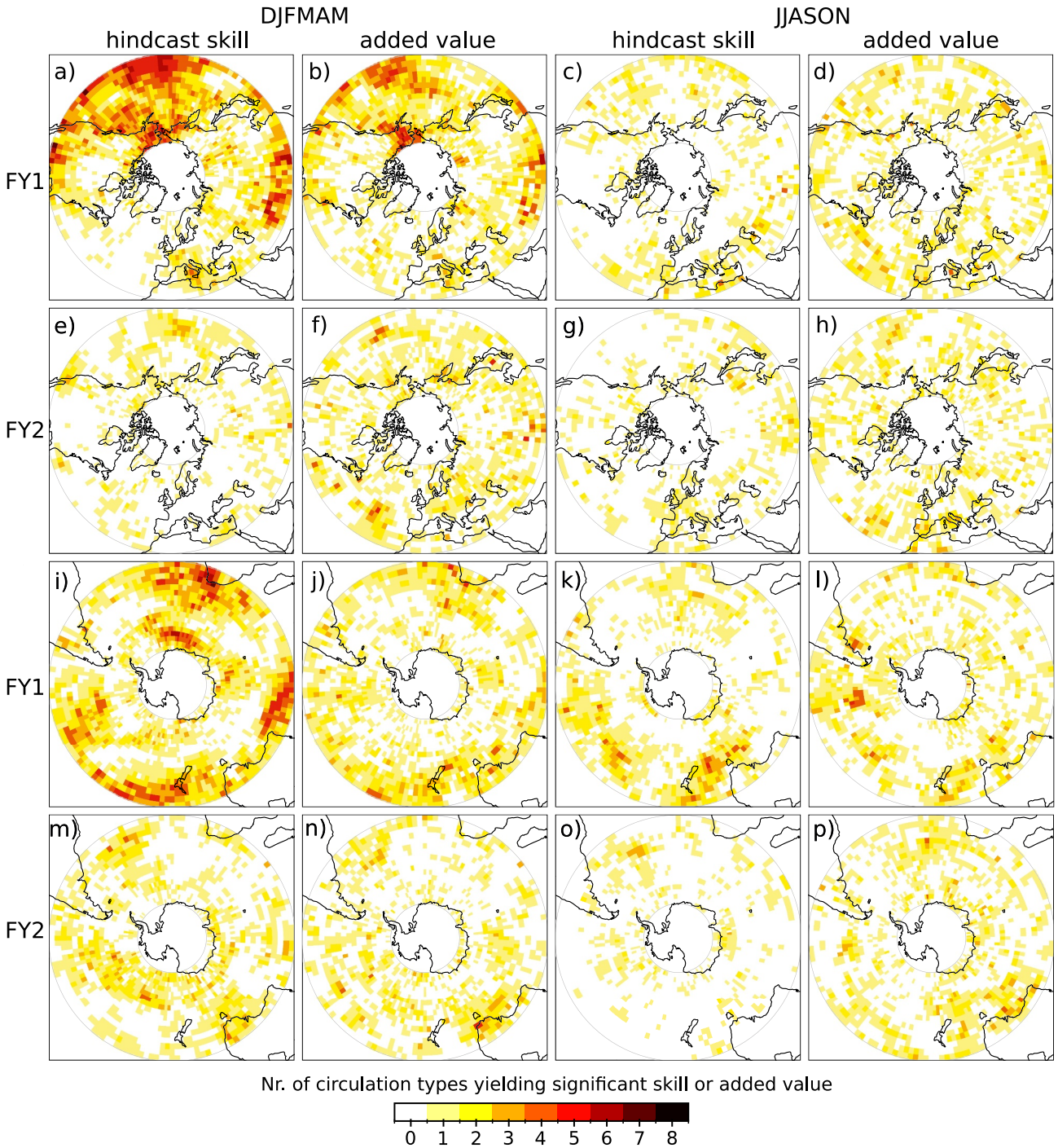

Figure 3. As Figure 1, but for the number of circulation types (out of 11) yielding significant skill (columns 1 and 3) or added value (columns 2 and 4).

weakly with the model's predictable component (r_m), indicating that the latter is only weakly associated with skill magnitude (second number). The RPC values of the historical experiment are also generally well below 1 (column 3).

As indicated by Figure S5 in Supporting Information S1, the spatial distribution of RPC values shifts toward positive values and a larger fraction >1 across all circulation types during the DJFMAM season in FY1 in both hemispheres (panels a and g). The largest spatial average RPC value is obtained for the westerly circulation type over the SH during the DJFMAM season in FY1 (g). However, even in this case, point-wise values rarely exceed

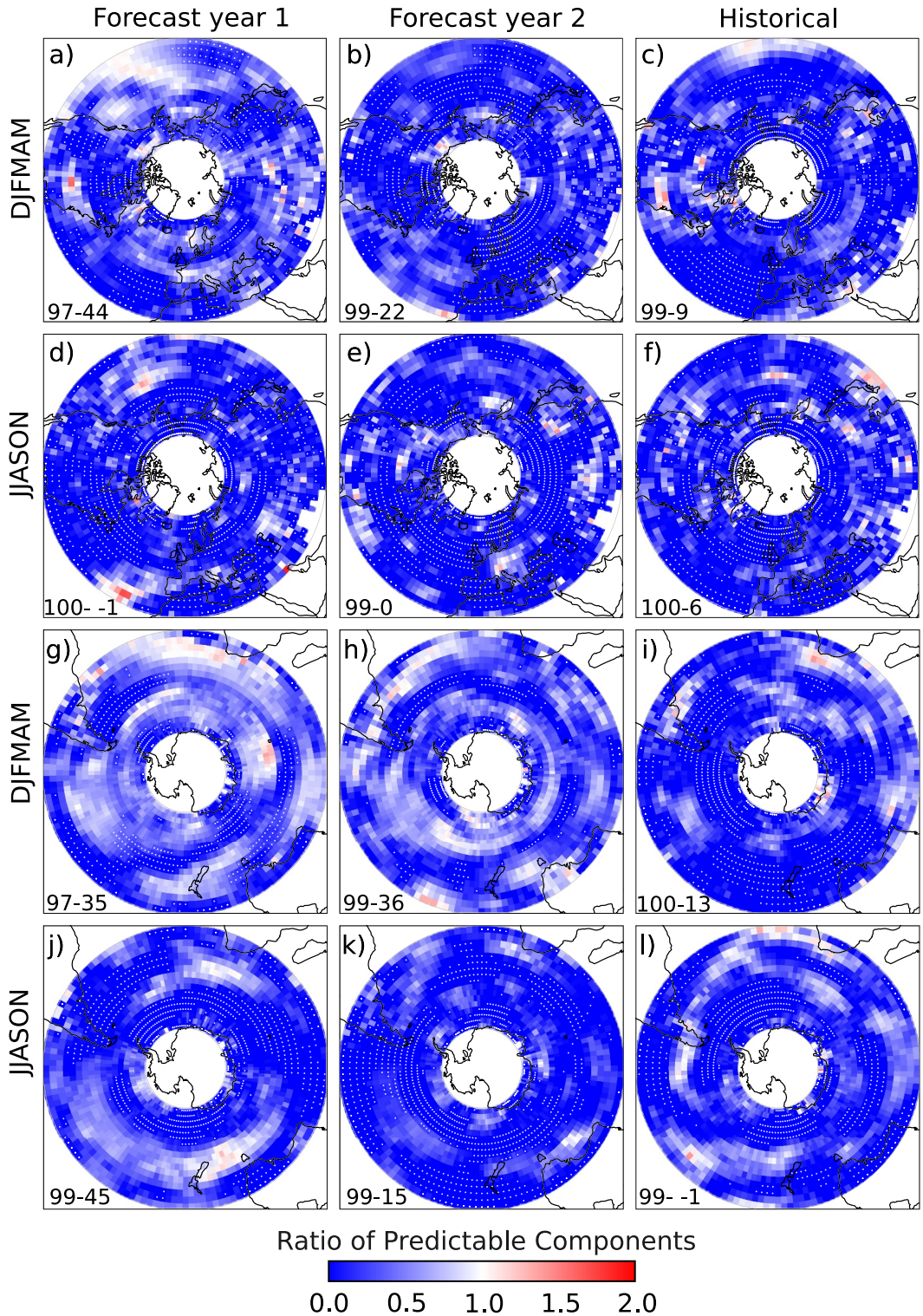

Figure 4. RPC for the semiannual frequencies of the westerly circulation type for FY1 and 2 from the dcppA ensemble (columns 1 and 2), the historical ensemble (column 3), DJFMAM and JJASON. White dots indicate significant differences between actual and potential predictability ($\alpha = 0.05$). Rows 1 and 2: Results for the NH, Rows 2 and 4: Results for the SH. Pattern correlation coefficients (×100) between the skill values shown in Figure 1 and the RCP (first number) or potential predictability (second number) as defined in Equation 3.2 are indicated in the lower left corner of the panels.

1. During FY2, the systematic shift toward positive values is still noticeable over the SH in DJFMAM (j), but disappears over the NH (d). RPC values for the JJASON season are centered around zero (d, e, and k), except for SH values in FY1 (j). As expected, RPC values for the historical experiment are generally centered around zero (column 3).

5. Discussion and Conclusions

We have assessed a 10-member ensemble of a fully initialized decadal forecasting system based on the EC-Earth3 coupled general circulation model (Bilbao et al., 2021), run with the dcppA-hindcast experimental protocol from CMIP6 (Boer et al., 2016), to evaluate its ability to reproduce observed semiannual occurrence frequencies of synoptic-scale atmospheric circulation types, as defined by Jenkinson and Collison (1977). Significant skill for at least 3 out of 11 circulation types is found over the Pacific North American sector, including the western North American coast and Alaska, as well as over the Southern Hemisphere (SH) extratropical ocean and adjacent land areas, such as Southeast Australia, New Zealand, and South Africa. This significant skill is confined to the DJFMAM season and persists for up to 13 months in lead time. For the JJASON season, significant skill is limited to the SH, with a lead-time of 7 months.

Potential sources of skill in the SH include circulation effects from stratospheric ozone forcing during austral summer (Arblaster & Meehl, 2006; Bracegirdle et al., 2020; Goyal et al., 2021; Ivanciu et al., 2021), the semi-annual oscillation in the circumpolar low-pressure trough (Schwerdtfeger, 1960; van Loon, 1967), and the persistence or propagation of stratospheric vortex anomalies to the troposphere from August to January, as documented by Byrne and Shepherd (2018). The Indian Ocean Dipole (IOD) also potentially contributes to the skill observed, particularly over southern Africa and Australia (Ummenhofer et al., 2009). ENSO teleconnections are relevant on seasonal to multi-year timescales in both hemispheres, particularly in the Pacific Ocean basin during the boreal winter season (Lenssen et al., 2024; Mo & Paegle, 2001; Younas & Tang, 2013). The correlation coefficient between the simultaneous Pacific North American (PNA) and Niño 3.4 indices during DJF, as reported by Li et al. (2019), is +0.53, constituting an upper predictability limit that aligns with the slightly weaker hindcast correlation values obtained here for the North Pacific sector.

Heterogeneous and mostly insignificant skill patterns were observed in the Northern Hemisphere (NH) outside the Pacific sector, suggesting that ENSO and sudden stratospheric warming signals propagating through stratosphere-troposphere coupling (Butler et al., 2016; Domeisen et al., 2019; Polvani et al., 2017), and North Atlantic sea surface temperature variations (Ummenhofer et al., 2017) do not provide systematic skill in the prediction system considered here. During JJASON, the obtained skill results are generally insignificant, which can be attributed to weaker ENSO teleconnections and the absence of the Arctic polar vortex during boreal summer (Hu et al., 2023).

In line with Falkena et al. (2022), the largest skill values are generally obtained for westerly circulation types, particularly in the SH. Westerly winds are crucial for the global climate system, as they steer the Antarctic Circumpolar Current (ACC) and the upwelling of carbon-rich deep water (Menviel et al., 2023; Sauvé et al., 2023). Therefore, it would be valuable to assess the predictability of SH carbon outgassing into the atmosphere using the carbon-cycle (CC) version of EC-Earth in future studies.

Data Availability Statement

The here applied EC-Earth3 and ERA5 data were retrieved from the ESGF data portals (Cinquini et al., 2012; Williams et al., 2016), https://esgf.llnl.gov, and from Copernicus Climate Data Store, https://cds.climate.copernicus.eu/datasets/reanalysis-era5-single-levels?tab=overview, respectively. The Python code underlying this study is publicly available from Brands (2025), https://github.com/SwenBrands/pyLamb, and https://github.com/zequihg50/smgdatatools.

Acknowledgments
This work has received funding from the European Union's Horizon Europe research and innovation programme under grant agreement No 101081555 (IMPETUS4CHANGE). SB acknowledges support by the Spanish MITECO and European Commission NextGenerationEU (Regulation EU 2020/2094), through CSIC's PTI-Clima. EC acknowledges support from Grant PRE2021-097646, funded by MICIU/AEI/10.13039/501100011033 and by ESF+.

References

Arblaster, J. M., & Meehl, G. A. (2006). Contributions of external forcings to southern annular mode trends. *Journal of Climate*, *19*(12), 2896–2905. https://doi.org/10.1175/JCLI3774.1

Baker, L. H., Shaffrey, L. C., Sutton, R. T., Weisheimer, A., & Scaife, A. A. (2018). An intercomparison of skill and overconfidence/underconfidence of the wintertime North Atlantic Oscillation in multimodel seasonal forecasts. *Geophysical Research Letters*, *45*(15), 7808–7817. https://doi.org/10.1029/2018GL078838

Bethke, I., Wang, Y., Counillon, F., Keenlyside, N., Kimmritz, M., Fransner, F., et al. (2021). NorCPM1 and its contribution to CMIP6 DCPP. *Geoscientific Model Development*, *14*(11), 7073–7116. https://doi.org/10.5194/gmd-14-7073-2021

Bilbao, R., Wild, S., Ortega, P., Acosta-Navarro, J., Arsouze, T., Bretonnière, P.-A., et al. (2021). Assessment of a full-field initialized decadal climate prediction system with the CMIP6 version of EC-Earth. *Earth System Dynamics*, *12*(1), 173–196. https://doi.org/10.5194/esd-12-173-2021

Boer, G. J., Smith, D. M., Cassou, C., Doblas-Reyes, F., Danabasoglu, G., Kirtman, B., et al. (2016). The decadal climate prediction project (DCPP) contribution to CMIP6. *Geoscientific Model Development*, *9*(10), 3751–3777. https://doi.org/10.5194/gmd-9-3751-2016

Bracegirdle, T. J., Holmes, C. R., Hosking, J. S., Marshall, G. J., Osman, M., Patterson, M., & Rackow, T. (2020). Improvements in circumpolar Southern Hemisphere extratropical atmospheric circulation in CMIP6 compared to CMIP5. *Earth and Space Science*, *7*(6), e2019EA001065. https://doi.org/10.1029/2019EA001065

Brands, S. (2022). A circulation-based performance atlas of the CMIP5 and 6 models for regional climate studies in the Northern Hemisphere mid-to-high latitudes. *Geoscientific Model Development*, *15*(4), 1375–1411. https://doi.org/10.5194/gmd-15-1375-2022

Brands, S. (2025). pyLamb - A climate model verification tool based on Lamb Weather Types. *Zenodo*. https://doi.org/10.5281/zenodo.15346362

Brands, S., Fernández-Granja, J. A., Bedia, J., Casanueva, A., & Fernández, J. (2023). A global climate model performance atlas for the Southern Hemisphere extratropics based on regional atmospheric circulation patterns. *Geophysical Research Letters*, *50*(10). https://doi.org/10.1029/2023GL103531

Brands, S., Herrera, S., & Gutiérrez, J. (2014). Is Eurasian snow cover in October a reliable statistical predictor for the wintertime climate on the Iberian Peninsula? *International Journal of Climatology*, *34*(5), 1615–1627. https://doi.org/10.1002/joc.3788

Butler, A. H., Arribas, A., Athanassiadou, M., Baehr, J., Calvo, N., Charlton-Perez, A., et al. (2016). The climate-system historical forecast project: Do stratosphere-resolving models make better seasonal climate predictions in boreal winter? *Quarterly Journal of the Royal Meteorological Society*, *142*(696), 1413–1427. https://doi.org/10.1002/qj.2743

Byrne, N. J., & Shepherd, T. G. (2018). Seasonal persistence of circulation anomalies in the Southern Hemisphere stratosphere and its implications for the troposphere. *Journal of Climate*, *31*(9), 3467–3483. https://doi.org/10.1175/JCLI-D-17-0557.1

Chang, E. K. M., Lee, S., & Swanson, K. L. (2002). Storm track dynamics. *Journal of Climate*, *15*(16), 2163–2183. https://doi.org/10.1175/1520-0442(2002)015⟨02163:STD⟩2.0.CO;2

Cinquini, L., Crichton, D., Mattmann, C., Harney, J., Shipman, G., Wang, F., et al. (2012). The Earth System Grid Federation: An open infrastructure for access to distributed geospatial data. In *2012 IEEE 8th international conference on E-science* (pp. 1–10). https://doi.org/10.1109/eScience.2012.6404471

Cottrell, F. M., Screen, J. A., & Scaife, A. A. (2024). Signal-to-noise errors in free-running atmospheric simulations and their dependence on model resolution. *Atmospheric Science Letters*, *25*(6), e1212. https://doi.org/10.1002/asl.1212

Deser, C., Phillips, A., Bourdette, V., & Teng, H. (2012). Uncertainty in climate change projections: The role of internal variability. *Climate Dynamics*, *38*(3–4), 527–546. https://doi.org/10.1007/s00382-010-0977-x

Domeisen, D. I., Garfinkel, C. I., & Butler, A. H. (2019). The teleconnection of el Niño southern oscillation to the stratosphere. *Reviews of Geophysics*, *57*(1), 5–47. https://doi.org/10.1029/2018RG000596

Döscher, R., Acosta, M., Alessandri, A., Anthoni, P., Arneth, A., Arsouze, T., et al. (2021). The EC-Earth3 Earth system model for the coupled model intercomparison project 6. *Geoscientific Model Development Discussions*, *2021*, 1–90. https://doi.org/10.5194/gmd-2020-446

Eade, R., Smith, D., Scaife, A., Wallace, E., Dunstone, N., Hermanson, L., & Robinson, N. (2014). Do seasonal-to-decadal climate predictions underestimate the predictability of the real world? *Geophysical Research Letters*, *41*(15), 5620–5628. https://doi.org/10.1002/2014GL061146

Eyring, V., Bony, S., Meehl, G. A., Senior, C. A., Stevens, B., Stouffer, R. J., & Taylor, K. E. (2016). Overview of the coupled model intercomparison project Phase 6 (CMIP6) experimental design and organization. *Geoscientific Model Development*, *9*(5), 1937–1958. https://doi.org/10.5194/gmd-9-1937-2016

Falkena, S. K., de Wiljes, J., Weisheimer, A., & Shepherd, T. G. (2022). Detection of interannual ensemble forecast signals over the North Atlantic and Europe using atmospheric circulation regimes. *Quarterly Journal of the Royal Meteorological Society*, *148*(742), 434–453. https://doi.org/10.1002/qj.4213

Fernández-Granja, J. A., Bedia, J., Casanueva, A., Brands, S., & Fernández, J. (2024). The signature of the main modes of climatic variability as revealed by the Jenkinson-Collison classification over Europe. *International Journal of Climatology*, *44*(11), 4076–4088. https://doi.org/10.1002/joc.8569

Fernández-Granja, J. A., Brands, S., Bedia, J., Casanueva, A., & Fernández, J. (2023). Exploring the limits of the Jenkinson–Collison weather types classification scheme: A global assessment based on various reanalyses. *Climate Dynamics*, *61*(3–4), 1829–1845. https://doi.org/10.1007/s00382-022-06658-7

Gillett, N. P., Shiogama, H., Funke, B., Hegerl, G., Knutti, R., Matthes, K., et al. (2016). The detection and attribution model intercomparison project (DAMIP v1.0) contribution to CMIP6. *Geoscientific Model Development*, *9*(10), 3685–3697. https://doi.org/10.5194/gmd-9-3685-2016

Goddard, L., Kumar, A., Solomon, A., Smith, D., Boer, G., Gonzalez, P., et al. (2013). A verification framework for interannual-to-decadal predictions systems. *Climate Dynamics*, *40*(1–2), 245–272. https://doi.org/10.1007/s00382-012-1481-2

Goyal, R., Sen Gupta, A., Jucker, M., & England, M. H. (2021). Historical and projected changes in the Southern Hemisphere surface westerlies. *Geophysical Research Letters*, *48*(4), e2020GL090849. https://doi.org/10.1029/2020GL090849

Hasselmann, K. (1976). Stochastic climate models part i. Theory. *Tellus*, *28*(6), 473–485. https://doi.org/10.1111/j.2153-3490.1976.tb00696.x

Hasselmann, K. (1979). On the signal-to-noise problem in atmospheric response studies. In (*Meteorology over the tropical oceans*). : Royal Meteorological Society.

Hersbach, H., Bell, B., Berrisford, P., Hirahara, S., Horányi, A., Muñoz-Sabater, J., et al. (2020). The ERA5 global reanalysis. *Quarterly Journal of the Royal Meteorological Society*, *146*(730), 1999–2049. https://doi.org/10.1002/qj.3803

Hu, S., Zhang, W., Jin, F.-F., Hong, L.-C., Jiang, F., & Stuecker, M. F. (2023). Seasonal dependence of the Pacific–North American teleconnection associated with ENSO and its interaction with the annual cycle. *Journal of Climate*, *36*(20), 7061–7072. https://doi.org/10.1175/JCLI-D-23-0148.1

Ivanciu, I., Matthes, K., Wahl, S., Harlass, J., & Biastoch, A. (2021). Effects of prescribed CMIP6 ozone on simulating the Southern Hemisphere atmospheric circulation response to ozone depletion. *Atmospheric Chemistry and Physics*, *21*(8), 5777–5806. https://doi.org/10.5194/acp-21-5777-2021

Jenkinson, A., & Collison, F. (1977). *An initial climatology of gales over the North sea (vol. 62; Tech. Rep. No. 18)*. Meterololgical Office.

Jones, P. D., Harpham, C., & Briffa, K. R. (2013). Lamb weather types derived from reanalysis products. *International Journal of Climatology*, *33*(5), 1129–1139. https://doi.org/10.1002/joc.3498

Jones, P. D., Hulme, M., & Briffa, K. R. (1993). A comparison of Lamb circulation types with an objective classification scheme. *International Journal of Climatology*, *13*(6), 655–663. https://doi.org/10.1002/joc.3370130606

Laloyaux, P., de Boisseson, E., Balmaseda, M., Bidlot, J.-R., Broennimann, S., Buizza, R., et al. (2018). CERA-20C: A coupled reanalysis of the twentieth century. *Journal of Advances in Modeling Earth Systems*, *10*(5), 1172–1195. https://doi.org/10.1029/2018MS001273

Lamb, H. (1972). British Isles weather types and a register of daily sequence of circulation patterns 1861-1971. *Meteorological Office, Geophysical Memoir*, *116*, 1–85.

Lenssen, N., DiNezio, P., Goddard, L., Deser, C., Kushnir, Y., Mason, S. J., et al. (2024). Strong El Niño events lead to robust multi-year ENSO predictability. *Geophysical Research Letters*, *51*(12), e2023GL106988. (e2023GL106988 2023GL106988. https://doi.org/10.1029/2023GL106988

Li, X., Hu, Z.-Z., Liang, P., & Zhu, J. (2019). Contrastive influence of ENSO and PNA on variability and predictability of North American winter precipitation. *Journal of Climate*, *32*(19), 6271–6284. https://doi.org/10.1175/JCLI-D-19-0033.1

Mann, M., Steinman, B., & Miller, S. (2020). 01). Absence of internal multidecadal and interdecadal oscillations in climate model simulations. *Nature Communications*, *11*(1), 49. https://doi.org/10.1038/s41467-019-13823-w

Meinshausen, M., Nicholls, Z. R. J., Lewis, J., Gidden, M. J., Vogel, E., Freund, M., et al. (2020). The shared socio-economic pathway (SSP) greenhouse gas concentrations and their extensions to 2500. *Geoscientific Model Development*, *13*(8), 3571–3605. https://doi.org/10.5194/gmd-13-3571-2020

Meinshausen, M., Vogel, E., Nauels, A., Lorbacher, K., Meinshausen, N., Etheridge, D. M., et al. (2017). Historical greenhouse gas concentrations for climate modelling (CMIP6). *Geoscientific Model Development*, *10*(5), 2057–2116. https://doi.org/10.5194/gmd-10-2057-2017

Menviel, L. C., Spence, P., Kiss, A. E., Chamberlain, M. A., Hayashida, H., England, M. H., & Waugh, D. (2023). Enhanced southern ocean {\mathrm{CO}}_{2} outgassing as a result of stronger and poleward shifted Southern Hemispheric westerlies. *Biogeosciences*, *20*(21), 4413–4431. https://doi.org/10.5194/bg-20-4413-2023

Mo, K. C., & Paegle, J. N. (2001). The Pacific–South American modes and their downstream effects. *International Journal of Climatology*, *21*(10), 1211–1229. https://doi.org/10.1002/joc.685

Philipp, A., Bartholy, J., Beck, C., Erpicum, M., Esteban, P., Fettweis, X., et al. (2010). Cost733cat – A database of weather and circulation type classifications. *Physics and Chemistry of the Earth, Parts A/B/C*, *35*(9), 360–373. (Classifications of Atmospheric Circulation Patterns – Theory and Applications). https://doi.org/10.1016/j.pce.2009.12.010

Polvani, L. M., Sun, L., Butler, A. H., Richter, J. H., & Deser, C. (2017). Distinguishing stratospheric sudden warmings from ENSO as key drivers of wintertime climate variability over the North Atlantic and Eurasia. *Journal of Climate*, *30*(6), 1959–1969. https://doi.org/10.1175/JCLI-D-16-0277.1

Sauvé, J., Gray, A. R., Prend, C. J., Bushinsky, S. M., & Riser, S. C. (2023). Carbon outgassing in the Antarctic Circumpolar Current is supported by Ekman transport from the sea ice zone in an observation-based seasonal mixed-layer budget. *Journal of Geophysical Research: Oceans*, *128*(11), e2023JC019815. https://doi.org/10.1029/2023JC019815

Scaife, A., & Smith, D. (2018). A signal-to-noise paradox in climate science. *npj Climate and Atmospheric Science*, *1*, 28. https://doi.org/10.1038/s41612-018-0038-4

Schwerdtfeger, W. (1960). The seasonal variation of the strength of the Southern Circumpolar Vortex. *Monthly Weather Review*, *88*(6), 203–208. https://doi.org/10.1175/1520-0493(1960)088⟨0203:TSVOTS⟩2.0.CO;2

Serras, F., Vandelanotte, K., Borgers, R., Van Schaeybroeck, B., Termonia, P., Demuzere, M., & Lipzig, N. (2024). 09). Optimizing climate model selection in regional studies using an adaptive weather type based framework: A case study for extreme heat in Belgium. *Climate Dynamics*, *62*(10), 9927–9949. https://doi.org/10.1007/s00382-024-07432-7

Smith, D., Eade, R., Scaife, A., Caron, L., Danabasoglu, G., DelSole, T., et al. (2019). Robust skill of decadal climate predictions. *npj Climate and Atmospheric Science*, *2*(1), 13. https://doi.org/10.1038/s41612-019-0071-y

Soares, P. M. M., Maraun, D., Brands, S., Jury, M. W., Gutiérrez, J. M., San-Martín, D., et al. (2019). Process-based evaluation of the VALUE perfect predictor experiment of statistical downscaling methods. *International Journal of Climatology*, *39*(9), 3868–3893. https://doi.org/10.1002/joc.5911

Trigo, R. M., & DaCamara, C. C. (2000). Circulation weather types and their influence on the precipitation regime in Portugal. *International Journal of Climatology*, *20*(13), 1559–1581. https://doi.org/10.1002/1097-0088

Ummenhofer, C. C., England, M. H., McIntosh, P. C., Meyers, G. A., Pook, M. J., Risbey, J. S., et al. (2009). What causes southeast Australia's worst droughts? *Geophysical Research Letters*, *36*(4), L04706. https://doi.org/10.1029/2008GL036801

Ummenhofer, C. C., Seo, H., Kwon, Y.-O., Parfitt, R., Brands, S., & Joyce, T. M. (2017). Emerging European winter precipitation pattern linked to atmospheric circulation changes over the North Atlantic region in recent decades. *Geophysical Research Letters*, *44*(16), 8557–8566. https://doi.org/10.1002/2017GL074188

van Loon, H. (1967). The Half-Yearly Oscillations in middle and high Southern Latitudes and the coreless winter. *Journal of the Atmospheric Sciences*, *24*(5), 472–486. https://doi.org/10.1175/1520-0469(1967)024⟨0472:THYOIM⟩2.0.CO;2

Wilks, D. S. (2006). *Statistical methods in the atmospheric sciences* (2nd ed., Vol. 91). Academic Press.

Williams, D. N., Balaji, V., Cinquini, L., Denvil, S., Duffy, D., Evans, B., et al. (2016). A global repository for planet-sized experiments and observations. *Bulletin of the American Meteorological Society*, *97*(5), 803–816. https://doi.org/10.1175/BAMS-D-15-00132.1

Wills, R. C. J., Dong, Y., Proistosecu, C., Armour, K. C., & Battisti, D. S. (2022). Systematic climate model biases in the large-scale patterns of recent sea-surface temperature and sea-level pressure change. *Geophysical Research Letters*, *49*(17), e2022GL100011. https://doi.org/10.1029/2022GL100011

Yeager, S., & Robson, J. (2017). Recent progress in understanding and predicting Atlantic decadal climate variability. *Current Climate Change Reports*, *3*(2), 1–16. https://doi.org/10.1007/s40641-017-0064-z

Younas, W., & Tang, Y. (2013). PNA predictability at various time scales. *Journal of Climate*, *26*(22), 9090–9114. https://doi.org/10.1175/JCLI-D-12-00609.1